Preface for Applied Scanning Probe Methods Vol. XI–XIII

The extremely positive response by the advanced community to the Springer series on Applied Scanning Probe Methods I–X as well as intense engagement of the researchers working in the field of applied scanning probe techniques have led to three more volumes of this series. Following the previous concept, the chapters were focused on development of novel scanning probe microscopy techniques in Vol. XI, characterization, i.e. the application of scanning probes on various surfaces in Vol. XII, and the application of SPM probe to biomimetics and industrial applications in Vol. XIII. The three volumes will complement the previous volumes I–X, and this demonstrates the rapid development of the field since Vol. I was published in 2004. The purpose of the series is to provide scientific background to newcomers in the field as well as provide the expert in the field sound information about recent development on a worldwide basis.

Vol. XI contains contributions about recent developments in scanning probe microscopy techniques. The topics contain new concepts of high frequency dynamic SPM technique, the use of force microscope cantilever systems as sensors, ultrasonic force microscopy, nanomechanical and nanoindentation methods as well as dissipation effects in dynamic AFM, and mechanisms of atomic friction.

Vol. XII contains contributions of SPM applications on a variety of systems including biological systems for the measurement of receptor–ligand interaction, the imaging of chemical groups on living cells, and the imaging of chemical groups on live cells. These biological applications are complemented by nearfield optical microscopy in life science and adhesional friction measurements of polymers at the nanoscale using AFM. The probing of mechanical properties by indentation using AFM, as well as investigating the mechanical properties of nanocontacts, the measurement of viscous damping in confined liquids, and microtension tests using in situ AFM represent important contributions to the probing of mechanical properties of surfaces and materials. The atomic scale STM can be applied on heterogeneous semiconductor surfaces.

Vol. XIII, dealing with biomimetics and industrial applications, deals with a variety of unconventional applications such as the investigations of the epicuticular grease in potato beetle wings, mechanical properties of mollusc shells, electro-oxidative lithography for bottom-up nanofabrication, and the characterization of mechanical properties of biotool materials. The application of nanomechanics as tools for the investigation of blood clotting disease, the study of piezo-electric

polymers, quantitative surface characterization, nanotribological characterization of carbonaceous materials, and aging studies of lithium ion batteries are also presented in this volume.

We gratefully acknowledge the support of all authors representing leading scientists in academia and industry for the highly valuable contribution to Vols. XI–XIII. We also cordially thank the series editor Marion Hertel and her staff members Beate Siek and Joern Mohr from Springer for their continued support and the organizational work allowing us to get the contributions published in due time.

We sincerely hope that readers find these volumes to be scientifically stimulating and rewarding.

August 2008

Bharat Bhushan
Harald Fuchs

19 A Review on the Structure and Mechanical Properties of Mollusk Shells – Perspectives on Synthetic Biomimetic Materials

*Francois Barthelat · Jee E. Rim · Horacio D. Espinosa**

Key words: Mollusk shells, Biomaterials, Fracture, Microfabrication, MEMS

19.1 Introduction

Natural materials can exhibit remarkable combinations of stiffness, low weight, strength, and toughness which are in some cases unmatched by manmade materials. In the past two decades significant efforts were therefore undertaken in the materials research community to elucidate the microstructure and mechanisms behind these mechanical performances, in order to duplicate them in artificial materials [1, 2]. This approach to design, called biomimetics, has now started to yield materials with remarkable properties. The first step in this biomimetic approach is the identification of materials performances in natural materials, together with a fundamental understanding of the mechanisms behind these performances (which has been greatly accelerated by recent techniques such as scanning probe microscopy).

The mechanical performance of natural materials is illustrated in Fig. 19.1, a material properties map for a selection of natural ceramics, biopolymer, and their composites [3]. The upper left corner of the map shows soft and tough materials such as skin, with a mechanical behavior similar to elastomers. The lower right corner of the chart shows stiff but brittle minerals such as hydroxyapatite or calcite. Most hard biological materials incorporate minerals into soft matrices, mostly to achieve the stiffness required for structural support or armored protection [4]. These materials are seen in the upper right part of the map and show how natural materials achieve high stiffness by incorporating minerals while retaining an exceptional toughness. Alternatively, one can consider how natural materials turn brittle minerals into much tougher materials, in some cases only with a few percent additions of biopolymers. These materials have in general relatively complex structures organized over several length scales (hierarchical structures [1, 2]) with mechanisms operating over several length scales, down to the nanoscale [5, 6].

Mollusk shells, the topic of this chapter, are an excellent example of such high-performance natural materials. Mollusks are composed to at least 95% of minerals

* Corresponding author

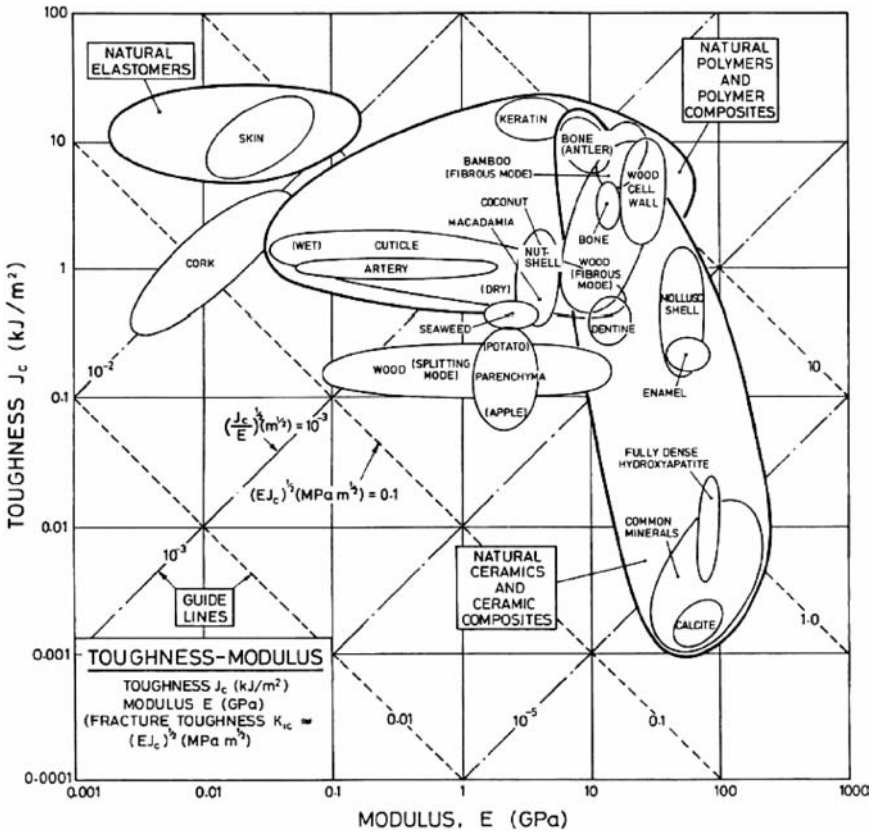

Fig. 19.1. Materials property map for a variety of ceramics, soft natural tissues, and their composites. The vertical axis (toughness) is a measure of the ability of the material to resist cracking, while the horizontal axis (modulus) is a measure of the stiffness of the material. Reproduced with permission from [3]

such as calcium carbonate (calcite, aragonite), yet by comparison with these brittle materials, mollusk shells are about 1,000-times tougher (see Fig. 19.1), at the expense of a small reduction in stiffness. How is such performance achieved? Can it be duplicated in artificial materials? This chapter gives first an overview of mollusk evolution and general characteristics. The next two parts then focus on the detailed structure and mechanics of two of the materials found in shells: the calcitic Pink Conch shell and Nacre from Red Abalone. Finally, the intricate structures and mechanisms of these materials have already inspired artificial materials, which are discussed in the last part of the chapter.

19.1.1 Mollusk Shells: Overview

Mollusks appeared 545 million years ago, and comprise about 60,000 species [7]. They have a very soft body (*mollis* means soft in Latin) and most of them grow

a hard shell for protection. The earlier mollusks were small (2–5 mm) with shell structures very similar to the modern forms. The size and the diversity of the mollusk family increased dramatically 440–500 millions years ago, with the apparition of various classes. Currently, the class that includes the largest number of species is the Gastropoda, with about 35,000 living species. These include mostly marine species (Conch shell, top shell, abalone), but also land species (land snails). The second largest class, the Bivalvia, counts about 10,000 species and includes clams, oysters, and freshwater mussels.

The shell of mollusks is grown by the mantle, a soft tissue that covers the inside of the shell. A great variety of shell structures has emerged from this process. They include prismatic, foliated and cross lamellar structure, columnar and sheet nacre (Fig. 19.2). All of these structures use either calcite or aragonite, with a small amount of organic material that never exceeds 5% of the composition in weight. In order to provide an efficient protection, the shell must be both stiff and strong. Mechanical tests on about 20 different species of seashells by Currey and Taylor [8] revealed an elastic modulus ranging from 40 to 70 GPa, and a strength in the 20–120-MPa range. By comparison, human femoral bone is softer ($E = 20$ GPa) but stronger (150–200-MPa strength). Amongst all the structures found in shells, nacreous structures appear to be the strongest: The strength of nacre can reach 120 MPa for the shell Turbo, as opposed to a maximum of 60 MPa for other non-nacreous structures.

The shells of mollusks offer a perfect example of a lightweight, tough armor system, that now serve as models for new armor designs. The structure and mechanical properties of the materials that compose these shells are of particular interest, and they are the focus of numerous studies.

19.2 Cross-Laminar Shells: The Pink or Queen Conch (*Strombus gigas*)

19.2.1 Structure

The giant pink conch or *Strombus gigas* is part of the *conus* family of shells. The conch shell has a logarithmic spiral shape, and exhibits the highest level of structural organization among mollusk shells. The shell has a particularly high ceramic content of 99 wt.%, composed of lath-like aragonite crystals arranged in a crossed-lamellar or ceramic "plywood" structure. The crossed-lamellar structure is the most common structure in mollusk shells, represented in ∼90% of gastropods and ∼60% of bivalves. While nacre with the brick and mortar microstructure exhibits the highest tensile and compressive strengths among the various mollusk shell micro-architectures, the crossed-lamellar structure is associated with the highest fracture toughness.

The conch shell is arranged in a laminated micro-architecture over five different length scales: the macroscopic layers, the first, second, and third-order lamellae, and internal twins within each third-order lamella. The three macroscopic layers are termed the inner (I) (closest to the animal), middle (M), and outer (O) layers. Each

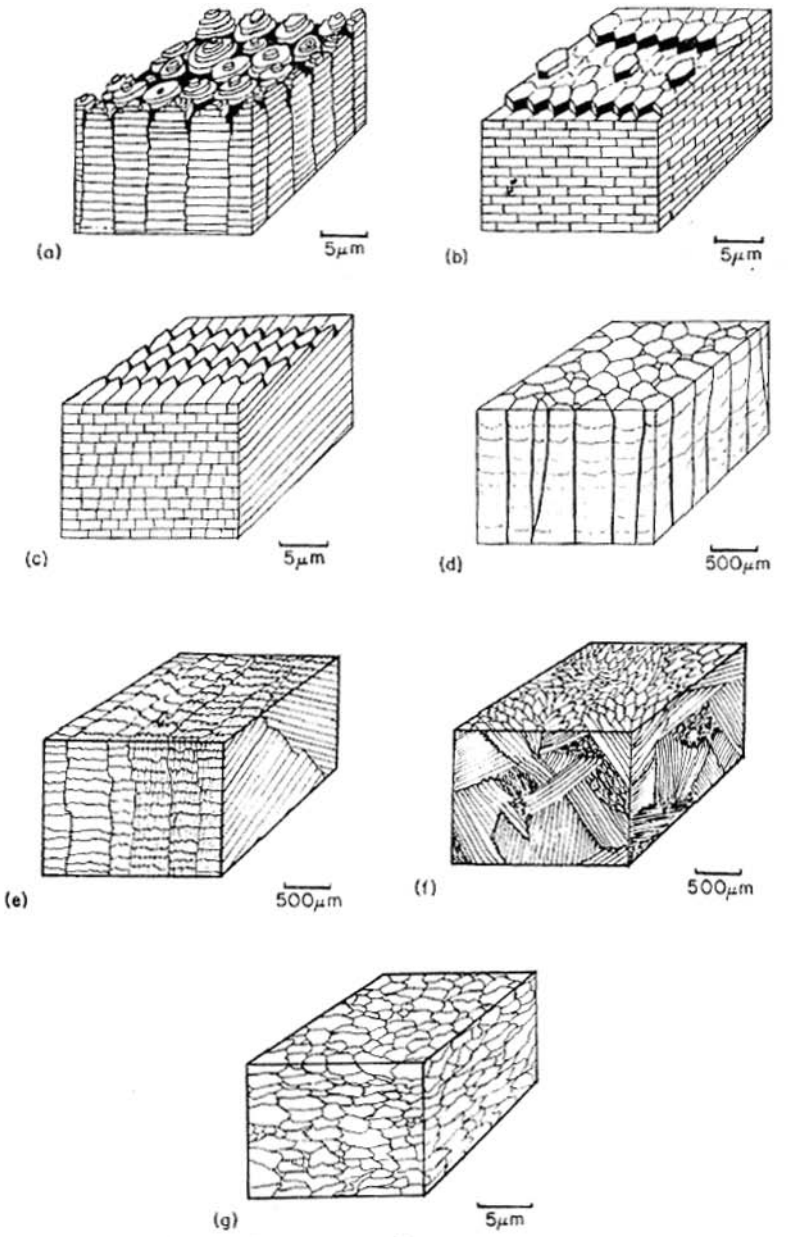

Fig. 19.2. Mineral structures found in seashells. (**a**): Columnar nacre. (**b**): Sheet nacre. (**c**): Foliated. (**d**): Prismatic. (**e**): Cross-Lamellar. (**f**): Complex crossed-lamellar. (**g**): Homogeneous. Reproduced with permission from [8]

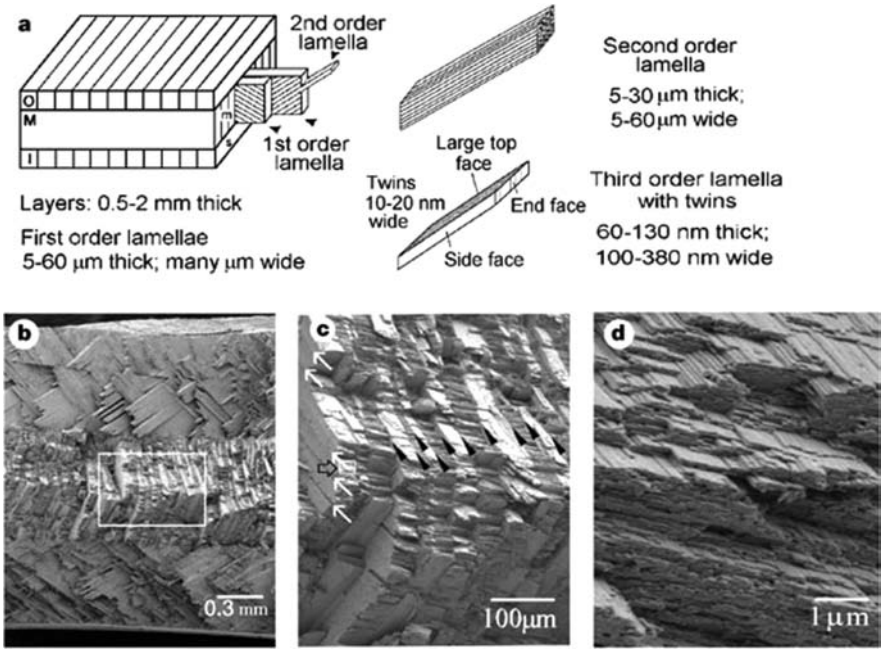

Fig. 19.3. Micro-architecture of the shell of *Strombus gigas*. (**a**) A schematic drawing of the crossed-lamellar structure, with characteristic dimensions of the three lamellar orders. (**b**), (**c**), and (**d**) SEM images of the fracture surface of a bend specimen at increasing magnification. Reproduced with permission from [9]

macroscopic layer is composed of parallel rows of first-order lamellae, and the first-order lamellae in the middle layer are oriented ∼90° to the first-order lamellae in the inner and outer layers. Each first-order lamella in turn is composed of parallel rows of second-order lamellae, which are oriented ∼45° to the first-order lamellae. The second-order lamellae are further subdivided into third-order lamellae. The basic building blocks are therefore the third-order lath-shaped aragonite crystals with internal twins. In particular, in the middle layer, the second-order lamellae in alternating first-order lamellae are rotated by ∼90°. The hierarchy of structural features and their characteristic dimensions are shown in Fig. 19.3(a). Each first, second, and third-order lamellae are enveloped in a thin organic matrix that composes only ∼1 wt. % of the shell [9–11].

Scanning electron microscope (SEM) images of fracture surfaces of bend test specimens are shown in Fig. 19.3(b)–(d), at increasing magnifications. They show clearly the three macroscopic layers [Fig. 19.3(b)] and the first, second and third-order lamellae and their relative orientations [Fig. 19.3(c)–(d)] [9].

19.2.2 Mechanisms of Toughening

The crossed-lamellar shells of *Strombus gigas* have an elastic modulus of 50 GPa, high bending strengths of 100 MPa, and an extremely high work of fracture up

to $13 \times 10^3 \, \mathrm{J/m^2}$ [11, 13]. The work of fracture is defined as the area under the load-displacement curve divided by the fracture surface area. The large work of fracture is achieved through two energy dissipating mechanisms – multiple tunnel cracks along the first-order interfaces in the inner (or outer) layer, and crack bridging of the first-order lamellae once the cracks start to grow through the middle layer.

Figure 19.4 shows the visual appearance of a bending test specimen under progressively larger loads [12]. During bending deformation, multiple tunnel cracks develop at the interfaces between the first-order lamellae in the inner or outer layers (the layer experiencing tension). These cracks are arrested at the interface with the middle layer, and are due to the existence of weak proteinaceous interfaces between the first-order lamellae. As the load increases, one or more of these cracks progress into the middle layer along the organic interfaces, but the crack propagation is resisted by bridging forces due to the first-order lamellae with second-order interfaces perpendicular to the crack surfaces. This large-scale bridging is the dominant energy dissipation mechanism.

Multiple crack formation in the weaker inner (or outer) layer during fracture leads to enhanced energy dissipation. This has been modeled using a two-layer, elastically homogeneous structure with fracture toughnesses of $K_c{}^m$ for the middle layer, and $K_c{}^i$ for the inner layer [14]. $K_c{}^i$ represents the fracture toughness of the proteinaceous interfaces between first-order aragonitic lamellae, while $K_c{}^m$ represents an effective toughness associated with the extension of tunnel cracks into the middle layer. It was shown using energetic arguments that for $K_c{}^m > 2K_c{}^i$, multiple cracks will develop in the inner layer under uniform tension, preventing the first crack from causing failure of the specimen. The experimentally observed values for $K_c{}^m/K_c{}^i$ are in the

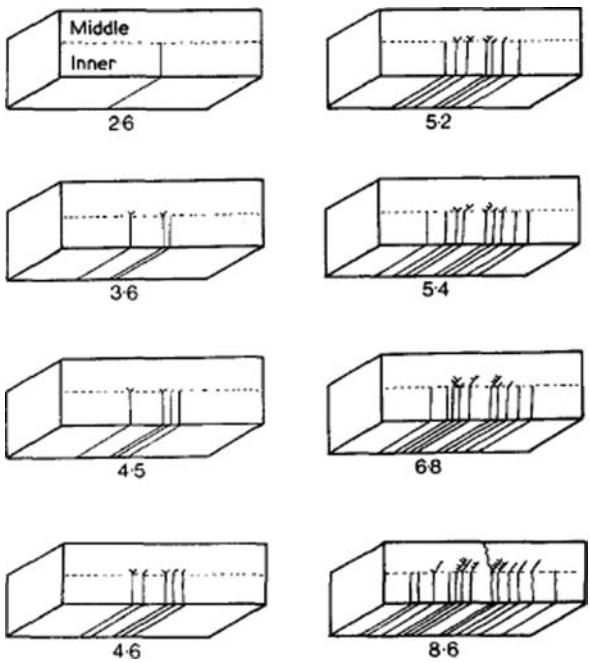

Fig. 19.4. Diagram of visual appearance of a test specimen under progressively greater loads. The loads are indicated in the figure in kg load. The lower surface is under tension. The cracks travel immediately to the junction of the inner and middle layers shown by the *dotted line*, but progress into the middle layer only with difficulty. Reproduced with permission from [12]

range 2.5–3.0 [9]. The interaction between the multiple closely spaced cracks leads to mutual shielding and thus a lower stress intensity factor at each crack tip compared to a specimen with a single crack. This in turn leads to a higher failure stress and strain, increasing the work of fracture.

However, multiple cracking accounts for a relatively small fraction of the toughness; a larger portion of the energy dissipated during fracture is associated with the crack bridging and microcracking in the tougher middle layer. The enhanced toughening is due to the alternating $\pm 45°$ orientation of the second-order lamellae in the middle layer, which forces the crack to bifurcate at the interface between the inner and middle layers as seen in Fig. 19.5. The tunnel cracks start to propagate through the middle layer along the weak interfaces between the second-order lamellae, but they are retarded by the bridging action of the first-order lamellae with second-order interfaces perpendicular to the crack surfaces. Figure 19.6 depicts the crack bridging analogous to fiber bridging in fibrous composites with frictional sliding at fiber–matrix interfaces [15].

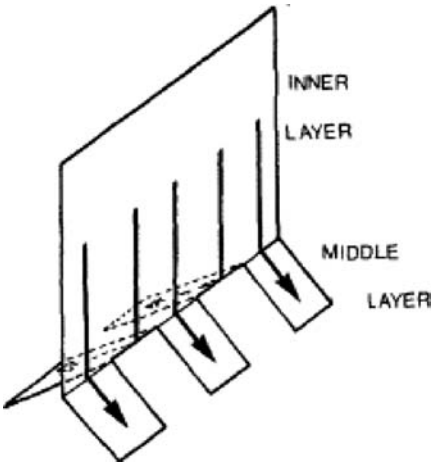

Fig. 19.5. Schematic of the geometry of crack growth at the interface between the inner and middle layers. Reproduced with permission from [12]

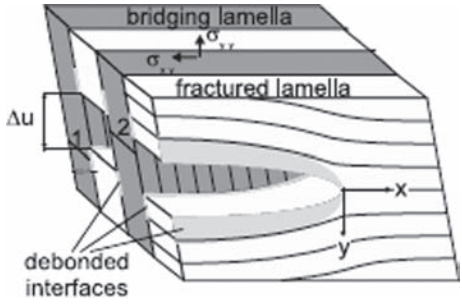

Fig. 19.6. Bridging with frictional sliding along debonded interfaces between fractured and bridging first-order lamellae. The low toughness second-order interfaces in the bridging lamellae are oriented perpendicular to the direction of crack propagation in the fractured lamellae. Reproduced with permission from [16]

Although the details of this mechanism have not been completely characterized, an approximate crack-bridging model was developed by Kamat et al. [9, 16]. The cohesive law of the crack bridging according to their micromechanical model is given by

$$\sigma(\Delta u) = \beta \Delta u^2, \tag{19.1}$$

where σ is the traction on the crack surfaces and Δu is the crack opening displacement. β is an effective parameter that incorporates all possible energy-dissipating mechanisms. The additional energy release rate associated with crack bridging is then given as

$$J_b = \int_0^{\Delta u_{cr}} \sigma(\Delta u) d\Delta u = \frac{2}{3} \beta {\Delta u_{cr}}^{3/2}, \tag{19.2}$$

where Δu_{cr} is the critical crack opening displacement. Experiments yielded parameter values of the model as $\beta = 630\,\mathrm{M/mm^{5/2}}$, $\Delta u_{cr} = 5\,\mu\mathrm{m}$, and $J_b = 148\,\mathrm{N/m}$ [16].

The crack bridging results in a work of fracture two orders of magnitude larger than that of monolithic aragonite [16]. Kamat et al. also demonstrated that the intrinsic material length scales of the shell design is such that it enables the shell to approach the favorable Aveston–Cooper–Kelly (ACK) limit, where the crack-bridging fibers remain intact as cracks propagate across the specimen [17].

The organic material at the interfaces play a large role in determining the toughness of the shell, which was found by varying the ductility of the organic phase [16]. At lower temperatures (–120 °C), the fracture behavior was brittle with relatively smooth fracture surfaces, indicating a small amount of fiber pullout and bridging, while at higher temperatures (80 °C), significant pullout and associated ductility of the specimen was observed. This demonstrates that the ductility of the proteinaceous phase at the interfaces is critical in achieving the high toughness of the shell. However, the exact mechanism by which this is achieved has not been fully quantified.

In summary, the mechanical advantage of the highly organized crossed-lamellar structure is an increased fracture resistance. The relatively weak and ductile interfaces together with a hierarchical laminated microstructure at several length scales make this possible through a combination of energy-dissipation mechanisms such as multiple cracking and crack bridging.

19.3 Nacreous Shells

Nacre from seashell is another example showing how evolution can lead to a high-performance material made out of relatively weak constituents. Nacre can be found inside many species of seashells from the gastropod and bivalve groups [Fig. 19.7(a)]. Nacre is mostly made of a mineral (aragonite $CaCO_3$, 95% vol.), arranged together with a small amount (5% vol.) of softer organic biopolymers [1].

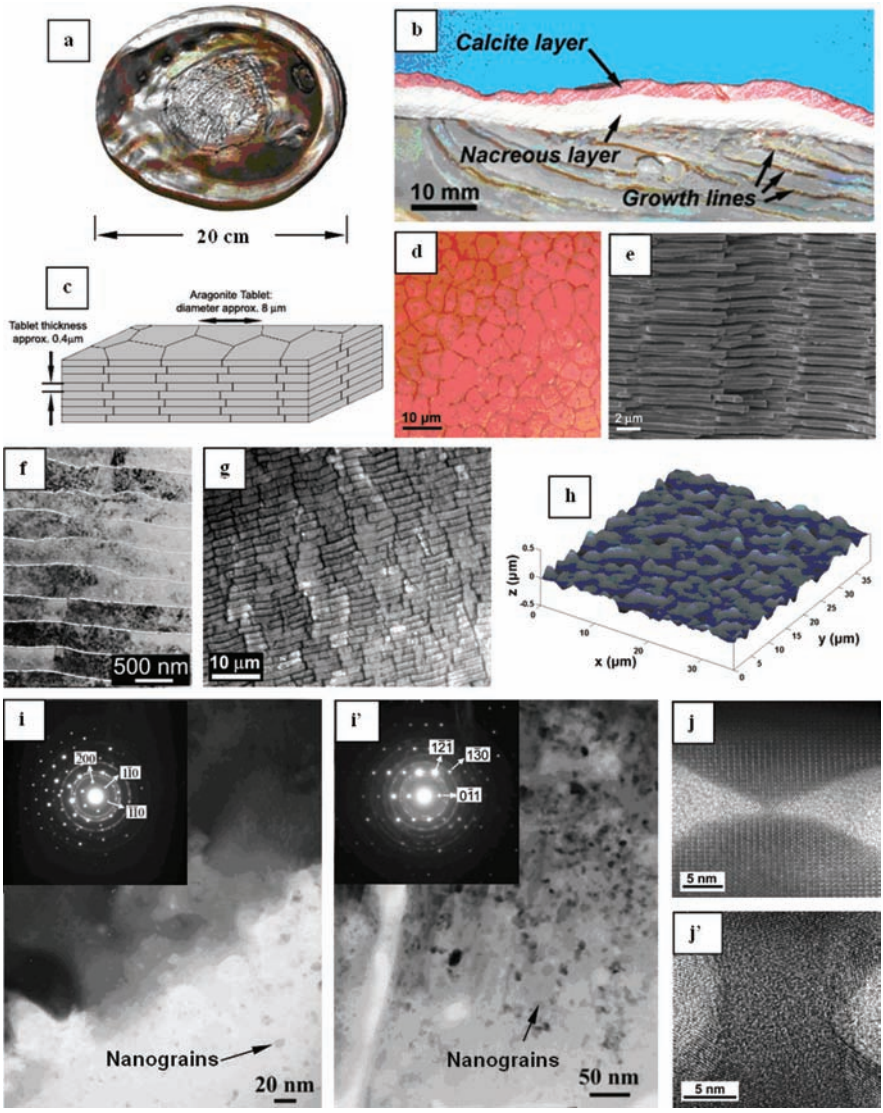

Fig. 19.7. The multiscale structure of nacre (all images from red abalone except **g**. (**a**) Inside view of the shell. (**b**) Cross section of a red abalone shell. (**c**) Schematic of the brick wall-like microstructure. (**d**) Optical micrograph showing the tiling of the tablets. (**e**) SEM of a fracture surface. (**f**) TEM showing tablet waviness (red abalone). (**g**) Optical micrograph of nacre from fresh water mussel (*Lampsilis cardium*). (**h**) Topology of the tablet surface from laser profilometry. (**i, i′**) TEM images showing a single aragonite crystal with some nanograins (*rings* on the SAD). (**j, j′**) HRTEM of aragonite asperity and bridge

While mostly made of aragonite, nacre is 3,000-times tougher than that material [3]. The structures and mechanisms behind this remarkable performance are examined in this section.

19.3.1 Overview of Nacre

Nacre is a highly complex biocomposite which, although made of a brittle mineral, is remarkably tough. Numerous mechanical experiments and models were therefore used to pinpoint which microstructural features are behind this performance, in order to duplicate them in artificial materials. It is now widely recognized that tablet sliding is a key mechanism in the toughness of nacre [18–21]. Because this mechanism is controlled by the interface between the tablets, many efforts have focused on investigating nanoscale mechanisms between the tablets [19, 22–25]. More recently, it was shown that these nanoscale mechanisms, while necessary, are not sufficient to explain the behavior of nacre at the macroscale [21]. Another key mechanism is actually found at the microscale, where the waviness of tablets generates progressive locking, hardening, and spreading of non-linear deformation around cracks and defects. The associated viscoplastic energy dissipation at the interfaces between tablets greatly enhances the toughness of nacre, arresting cracks before they become a serious threat to the shell and to the life of the animal. Nacre is therefore a perfect example of a natural material which developed a highly sophisticated microstructure for optimal performance, over millions of years of evolution. The structure and mechanisms of this remarkable material are now inspiring the design of the next generation of synthetic composites material.

19.3.2 Structure

Like the Pink Conch and many other biological materials, nacre has a hierarchical structure, meaning that specific structural features can be found at distinct length scales. At the millimeter scale the shell consists of a two-layer armor system, with a hard outer layer (large calcite crystals) and a softer but more ductile inner layer [nacre, Fig. 19.7(a), (b)]. Under external mechanical aggressions the hard calcite layer is difficult to penetrate, but is prone to brittle failure. Nacre, on the other hand, is relatively ductile and can maintain the integrity of the shell even if the outer layer is cracked, which is critical to protect the soft tissues of the animal. This design of hard ceramic used in conjunction with a softer backing plate is believed to be an optimal armor system [1]. Furthermore, within the nacreous layer itself there are a few sub-layers of weaker material, the so-called growth lines [26] which may act as crack deflectors [27].

The microscale architecture of nacre resembles a three-dimensional brick and mortar wall, where the bricks are densely packed layers of microscopic aragonite polygonal tablets (about 5–8 μm in diameter for a thickness of about 0.5 μm) held together by 20–30-nm thick layers of organic materials [Fig. 19.7(c)–(e)]. The tablets

in nacre from abalone shell and other gastropods are arranged in columns (*columnar nacre*), while the tablets in nacre from bivalve such as mussels or oyster are arranged in a more random fashion (*sheet nacre*). Remarkably, the arrangement and size of the tablets in nacre is highly uniform throughout the nacreous layer. Optical microscopy on a cleaved nacre surface reveals Voronoi-like contours [Fig. 19.7(d)], with no particular orientation within the plane of the layer.

While the tablets are generally described and modeled as flat at the microscale [20, 22], they actually exhibit a significant waviness [28]. This feature could be observed using optical microscopy, scanning probe microscopy, and scanning and transmission electron microscopy. Tablet waviness is not unique to nacre from red abalone [Fig. 19.7(f)]; it was also observed on another gastropod species [top shell *Trochus niloticus*, Fig. 19.7(h)], and in a bivalve [freshwater mussel *Lampsilis Cardium*, Fig. 19.7(g)]. The waviness of the tablets can be also observed for many other species in the existing literature [1, 29–33]. For the case of red abalone laser profilometry was used to measure a roughness (RMS) of 85 nm, for an average peak-to-peak distance of 3 μm [21]. The roughness can reach amplitudes of 200 nm, which is a significant fraction of the tablet thickness [450 nm, Fig. 19.7(f)–(h)] [21]. The waviness of the tablets is highly conformal so that the tablets of adjacent layers fit perfectly together.

Nacre exhibits structural features down to the nanoscale. While transmission electron microscopy suggest that the tablets are made of large aragonite grains with a few inclusions of nanograins [Fig. 19.7(i), (i′)] [1, 34], recent scanning probe microscopy observations suggests that the tablet are nanostructured, with grains in the 30-nm range [35, 36]. These nanograins all have the same texture and they are delimited by a fine network of organic material [36]. At the 20–30-nm interfaces between the tablets, nanoscale features can also be found. The organic material that fills this space and bonds the tablets together is actually composed of several layers of various proteins and chitin [23, 37]. These sheets of organic layers contain pores with a 20–100-nm spacing, leaving space for two types of aragonite structures: nanoasperities [Fig. 19.7(j)] and direct aragonite connections across the interfaces [mineral “bridges” connecting tablets, Fig. 19.7(j′)]. These nanoscale features were observed using scanning probe microscopy [33, 34], scanning electron microscopy [19, 38], and transmission electron microscopy [24, 34, 38]. The height and width of these features varies from 10 to 30 nm while their spacing is in the order of 100–200 nm [34] The density, size, and shape of these asperities can vary significantly from one area to another (Fig. 19.8).

19.3.3 The Deformation of Nacre

The deformation behavior of nacre has been studied experimentally using a variety of configurations including uniaxial tension [21, 39, 40], uniaxial compression [34, 41], three- and four-point bending [18, 19], and simple shear [21]. The behavior of nacre at high strain rates was also explored [41]. Most of these tests were performed on millimeter-sized specimens. Smaller scale experiments were also used to determine the mechanical response of the individual components of nacre, including

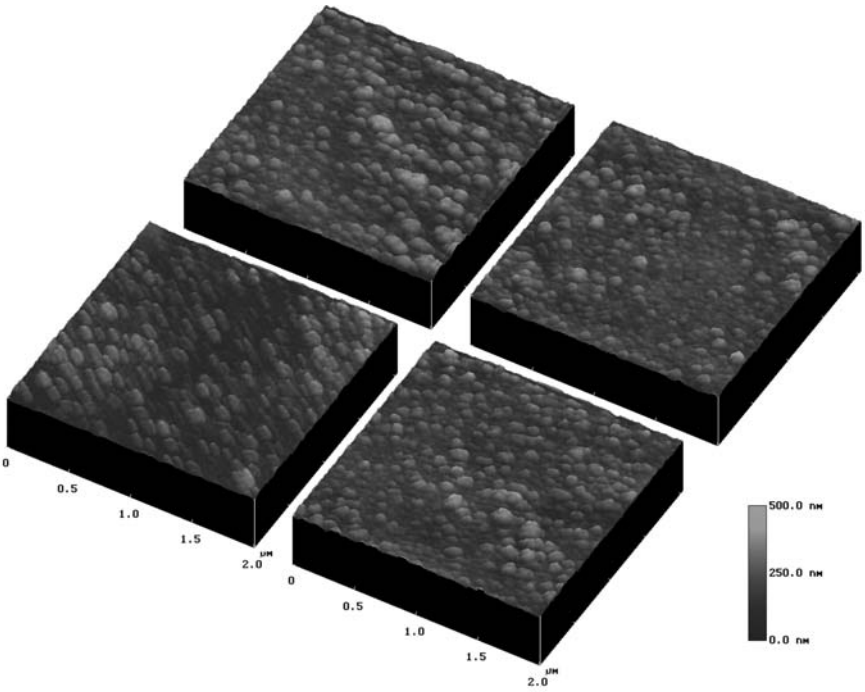

Fig. 19.8. 2×2-μm AFM scans from different areas of a cleaved specimen of nacre, showing the surface of the tablets. Asperities of various densities, heights, and shapes could be observed. Reproduced with permission from [28]

nanoindentation on single nacre tablets [33,34,42], and load-extension curves on single molecules of organic materials [23]. At the macroscale, the most striking mode of deformation is in uniaxial tension along the directions of the tablets (it is also the most relevant mode of deformation for nacre within the shell). Figure 19.9(a) shows the tensile behavior of nacre, showing some ductility at the macroscale [Fig. 19.9(a), (b)]. The stress-strain curve shows relatively large deformations, accompanied by hardening up to failure at a microscopic strain of almost 1%. Full strain field measurement revealed local strain values of 2% [40]. The transition from elastic to inelastic behavior is progressive (rounding of the curve), which probably results from the statistics of the microstructure. Unloading paths show a decrease in modulus, which indicates progressive accumulation of damage. The tensile behavior of aragonite is also shown on that graph: linear elastic deformation followed by sudden, brittle failure at small strains. Nacre, although made of 95% of that mineral, exhibit a ductile-like behavior with relatively large strain at failure.

This remarkable behavior is achieved by the following microscopic mechanism: At a tensile stress of about 60 MPa the interfaces start to yield in shear and the tablets slide on one another, generating local deformation. This phenomenon spreads over large volumes throughout the specimen, which translates into relatively large strains at the macroscale. Once the potential sliding sites are exhausted, the specimen fails

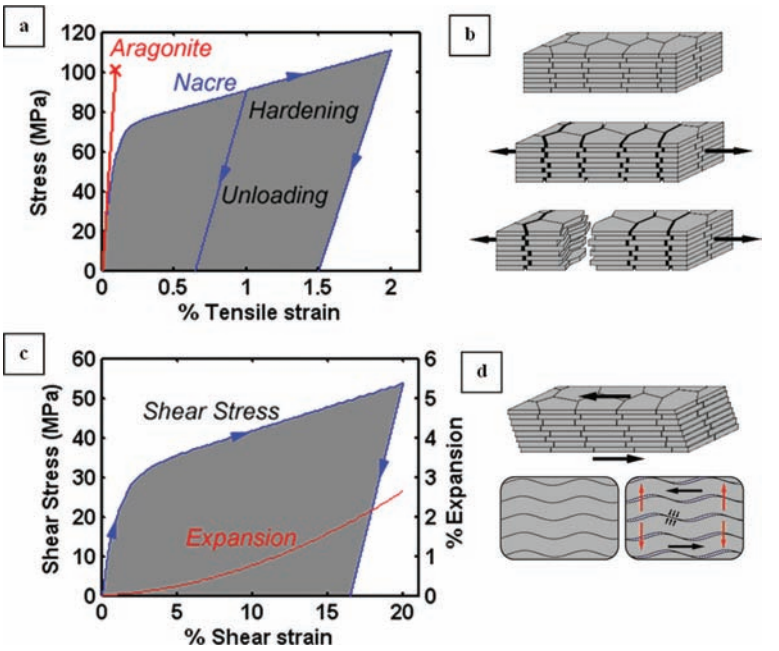

Fig. 19.9. (**a**) Experimental tensile stress-strain curve for nacre and (**b**) associated deformation modes. (**c**) Experimental shear stress-strain curve for nacre and (**d**) deformation mechanism. Tablet waviness generates resistance to sliding, accompanied by lateral expansion (*red arrows*)

by pullout of the tablets [see fracture surface, Fig. 19.7(e)], which occurs after local sliding distances of 100–200 nm. This type of micromechanism is unique to nacre, and it is the main source of its superior mechanical properties. For this reason numerous models were developed to capture this behavior [18, 20, 21, 43].

In order to achieve such behavior, however, some requirements must be met. First, the interface must be weaker than the tablets; otherwise, the tablets would fail in tension before any sliding could occur, which would lead to a brittle type of failure. Strong tablets are important in this regard, and it was shown that their small size confer them with increased tensile strength compared to bulk aragonite [5, 39]. It has also been suggested that the presence of nanograins provides some ductility to the tablets [44]. This would increase the tensile strength of the tablets, but would not significantly affect the deformation mode of nacre, which is dominated by tablet sliding. In addition, the aspect ratio of the tablets must be high enough to maximize sliding areas and produce strong cohesion within the material [45]. However, the aspect ratio is bounded by the fact that too thin tablets would lead to premature tablet failure and brittle behavior. Another fundamental requirement is that some hardening mechanism must take place at the local scale in order to spread sliding throughout the material. As tablets start to slide, higher stresses are required to slide them further so that it is more favorable for the material to initiate new sliding sites, thus spreading deformation over large volumes. Since the tablets

remain essentially elastic in this process, the hardening mechanism has to take place at the interfaces. The best approach to interrogate the behavior of the interface directly is a simple shear test along the layers [21]. The shear stress-strain curve reveals a very strong hardening and failure that occurred at shear strains in excess of 15% [Fig. 19.9(c)]. The full strain field, measured by image correlation techniques, also captured a significant *expansion* across the layers. This important observation suggested that the tablets have to climb some obstacles in order to slide on one another. Either in tension or shear, strain hardening is the key to large deformation and is essential to the mechanical performance of nacre.

From this observation it is clear that the performance of nacre is controlled by mechanisms at the interfaces between these tablets. In particular, it is important to identify which mechanisms generate resistance to shearing and hardening. Several nanoscale mechanisms were proposed (Fig. 19.10) and are discussed next.

First, the tough organic material at the interfaces [Fig. 19.10(a)] has an extremely strong adhesion to the tablets [18, 23]. Some of the molecules it contains include modules that can unfold sequentially under tensile load, enabling large extensions [23] and maintaining cohesion between tablets over long sliding distances. The load-extension curve of a single of these molecules shows a saw-tooth pattern, where each drop in load corresponds to the sequential unfolding of the molecule [23]. When a bundle of these molecules is considered, however, the unfolding processes would operate more or less at constant load. Only when all the modules have unfolded does the chain stiffen significantly (at least upon a 100-nm extension [23]). If this type of molecule is attached to adjacent tablets and ensures their cohesion, little hardening should be expected from them, at least in the first 100 nm or so of tensile or shear deformation of the interface. This type of extension is on the order of the sliding distance observed in nacre tensile specimens, and therefore no significant hardening could be generated by the polymer during the tensile deformation of nacre. In the simple shear test, however, the shear strains at the interface are much higher and the polymer may contribute significantly to the hardening observed at the macroscale.

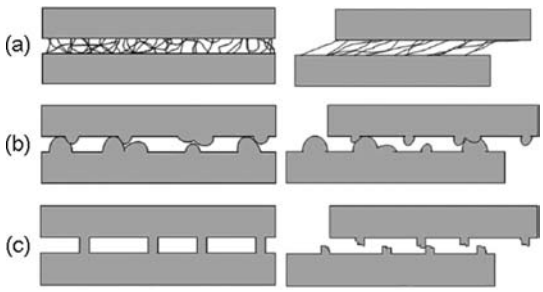

Fig. 19.10. Nanoscale mechanisms controlling the shearing of the tablet's interfaces: (**a**): Biopolymer stretching; (**b**): aragonite asperities contact; (**c**) aragonite bridges initially intact (*left*), and then showing some potential relocking after shearing (*right*). Adapted with permission from [25]

Another nanoscale mechanism is controlled by the nanoasperities on the surface of the opposed tablets, which may enter into contact and interact as the interface is sheared [Fig. 19.10(b)]. This mechanism was proposed as a source of strength and hardening at the interfaces [19, 22]. The strength of aragonite is sufficient for the nanoasperities to withstand contact stresses with very little plasticity [34]. However, the small size of these asperities restricts the range of sliding over which they provide hardening to about 15–20 nm [22], which is much smaller than the sliding of 100–200 nm observed experimentally. Beyond sliding distances of 15–20 nm, one must therefore assume that the resistance the nanoasperities provide remains constant (as shown in [22]).

The third nanoscale mechanism at the interface is associated with the aragonite bridges [Fig. 19.10(c)]. These bridges probably act as reinforcements for the interfaces, and probably influence the overall behavior of nacre [24]. However, given the brittleness of aragonite, they could not generate much resistance to tablet sliding after failure, which probably occurs at small interface shearing strains. After some sliding distance another mechanism was suggested, where broken bridges re-enter in contact, thereby generating re-locking of the tablets (Fig. 19.10(c) [25]). This mechanism has, however, not been demonstrated.

While the three nanoscale mechanisms described above contribute to the shearing resistance of the tablet interfaces, they cannot generate the level of hardening required for the spreading of non-linear deformations observed at the macroscale. In addition, none of these mechanisms could generate the transverse expansion associated with shearing of the layers [Fig. 19.9(c)].

A fourth mechanism was recently proposed where the hardening mechanism is generated by the waviness of the surfaces [21]. As the layers slide on one another in the simple shear tests, the tablets must climb each others waviness, which generates progressive tablet interlocking and an increasing resistance to sliding. In addition, such mechanisms could generate the observed transverse expansion, while the organic glue maintains the tablets together. While this mechanism can easily be envisioned in simple shear [Fig. 19.9(d)], it is less obvious in tension, because tablet sliding only occurs in the tablet overlap areas. Close examination actually reveals that waviness also generated locking in tension. Figure 19.11(a) shows an actual image

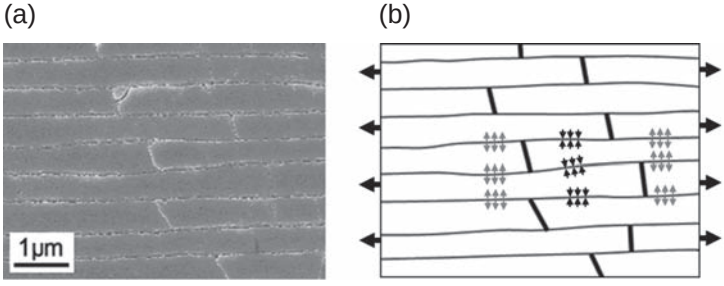

Fig. 19.11. (**a**) Scanning electron micrographs of a few dovetail-like features at the periphery of the tablets. (**b**) Outline of the tablets contours, showing some of the stresses involved when nacre is stretched along the tablets. In addition to shear the interface is subjected to normal compression (*black arrows*) which generates resistance to tablet pullout. Equilibrium of forces at the interfaces requires tensile tractions at the core of the tablets. Reproduced with permission from [40]

of the structure of nacre. Tablet waviness is evident, and it can be seen that it generates dovetail-like features at the end of some tablets. Such structure, loaded in tension, will generate progressive locking and hardening at large scales [Fig. 19.11(b)]. Microstructure-based three-dimensional finite element models have actually demonstrated that waviness was indeed the key feature that generated hardening in nacre [21]. Even though some of the nanoscale mechanisms of Fig. 19.10 are required to maintain cohesive strength between tablets, waviness is required for hardening. Such a hardening mechanism has a significant impact on the toughness of nacre, as described in the next section.

19.3.4 The Fracture of Nacre

Many flaws are present within nacre, for instance, porosity, Fig. 19.12(a), and defective growth, Fig. 19.12(b). These flaws are potential crack starters that can eventually lead to catastrophic failure under tensile loading [46]. For a material like nacre defects cannot be eliminated so the only alternative is to incorporate robustness in the material design such that cracks that might emanate from them are resisted. The resistance to cracking can be assessed with fracture testing [1, 18]. However, it was only recently that the full crack-resistance curve (toughness as a function of crack advance) was determined for nacre from red abalone [40] [Fig. 19.13(c)].

As the far field stress is increased on the fracture specimen, a white region appears and progressively increases in size [Fig. 19.13(a), (b)]. This whitening is an indication of tablet sliding and inelastic deformations, with the voids left by tablet separation scattering light (this phenomenon is similar to "stress whitening" associated with crazing in polymers). In the literature dealing with fracture mechanics, such an inelastic region is referred to as the *process zone* [46]. The process zone reaches about 1 mm in width [Fig. 19.13(b)] when the crack started to propagate at a J-integral value of $J_0 = 0.3\,\mathrm{kJ/m^2}$, which is already 30-times higher than

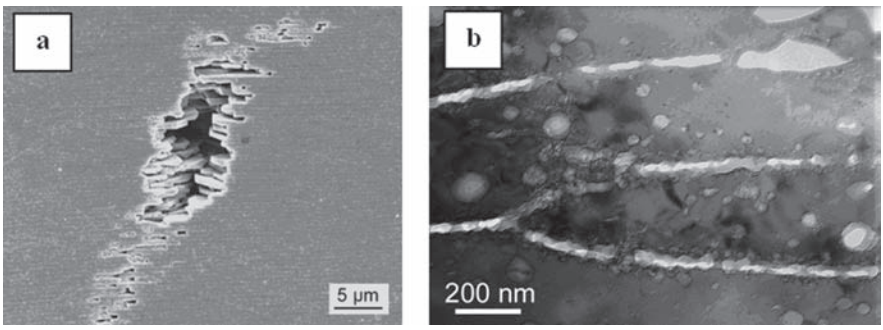

Fig. 19.12. (**a**) Large defect inside the nacreous layer (SEM). (**b**) "Stacking fault" in the tablet layers (TEM)

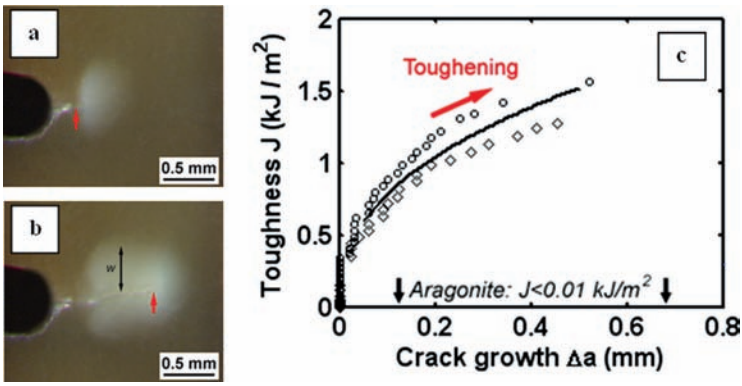

Fig. 19.13. (**a**) Prior to crack advance a tablet sliding zone develops ahead of the crack tip. (**b**) As the crack advances it leaves a wake of inelastically deformed material (**a** and **b**: optical images; *red arrow* shows location of crack tip at the onset of crack propagation and the steady state regime). (**c**) Crack resistance (J_R) curves for nacre from two experiments

the toughness of pure aragonite (about $0.01\,\mathrm{kJ/m^2}$). During the fracture test the crack propagated slowly in a very stable fashion that resembled tearing rather than the fast, catastrophic crack propagation typical to ceramics. On the crack-resistance curve the toughness increases significantly with crack advance Δa [Fig. 19.13(c)]. Such rising crack resistance curves have also been observed in dentin enamel [47] and bone [48]. Cracks in such materials tend to be very stable; upon propagation they tend to slow down and can even be arrested. The rising crack resistance curve and high toughness of nacre could be associated with the formation of the large, whitened region of inelastic deformation around the crack using fracture mechanics models [40].

By considering the energy dissipated upon an incremental crack extension or by straight use of the *J*-integral definition one can show that in the steady-state the initial (intrinsic) toughness J_0 is augmented by an energy dissipation term [46]:

$$J_{ss} = J_0 + 2\int_0^W U(y)dy \tag{19.3}$$

where w is the process zone width and $U(y)$ is the energy density, i.e., the mechanical energy (including dissipated and stored energies) per unit area per unit thickness in the z-direction, behind in the wake as $x \to \infty$ [49]. The analysis shares similarities with toughening in rubber-toughened polymers [50, 51] and toughening in transforming materials [49]. The exact calculation of $U(y)$ from strain fields requires accurate knowledge of the material constitutive law under multiaxial loading, including hysteretic unloading. Currently such constitutive description is only partially available for nacre. An estimate of the increase in J, in the steady-state, can be obtained, however, if one assumes that (1) the inelastic deformation associated with tablet sliding is the prominent energy dissipation and toughening mechanism

(i.e., the effects of shear and transverse expansion in the wake, as well as elastic energies trapped outside of the wake are neglected); (2) the stress σ_{yy} around the tip can be predicted from the uniaxial tensile response [Fig. 19.9(a)]; and (3) the residual strain ε_{yy} in the wake decreases linearly from the crack face to the edge of the wake, as suggested by experimental observations [Fig. 19.13(c)]. Then, the total J can be written as,

$$J_{ss} \approx J_0 + 2 \int_0^w \int_0^{\varepsilon_{yy}(y)} \sigma(\varepsilon) d\varepsilon dy \tag{19.4}$$

The upper bound of the inner integral, $\varepsilon_{yy}(y)$, is the residual strain across the direction of the crack at $x \to -\infty$ (which decreases linearly with y). The integration of the loading-unloading histories across the width of the wake [$2w = 1\,\mathrm{mm}$, Fig. 19.13(b)] yields an increase of toughness of $0.75\,\mathrm{kJ/m^2}$. Combined with the initial toughness, the predicted steady state toughness is therefore $1.05\,\mathrm{kJ/m^2}$. This value is lower than the experimental maximum toughness of about $1.6\,\mathrm{kJ/m^2}$ [Fig. 19.13(c)], but shows that dissipative energies associated to dilation and elastic deformation of the material surrounding the wake are significant contributors to the toughening of nacre. In comparison, the contributions of other mechanisms such as crack deflection or crack bridging [52, 53] are negligible. Note that this type of toughening is made possible by (1) spreading of non-linear deformations and (2) its associated energy dissipation.

19.4 Artificial Shell Materials

As described in Sects. 19.2 and 19.3, the attractive mechanical properties of mollusk shells such as nacre and conch shells have inspired a large class of biomimetic materials and organic–inorganic composites. The creation of artificial shell materials with their intricate microstructure is a challenge that requires both the design of optimum microstructures and the development of fabrication procedures to implement these designs. In the following section, we describe some of the efforts at mimicking the architecture of shell materials with different fabrication methods.

19.4.1 Large-Scale "Model Materials"

The challenge of trying to mimic the shell architecture at the $\mu\mathrm{m}$ level led to the development of model systems on the macroscopic scale [54, 55]. An important toughening mechanism of nacre is the crack deflection due to the presence of weak interfaces between the brittle aragonite tiles. Larger-scale segmented layered composites with ceramic tablets make use of this toughening mechanism to overcome the brittleness of ceramics.

Clegg et al. used thin square tiles ($50\,\mathrm{mm} \times 50\,\mathrm{mm} \times 200\,\mu\mathrm{m}$) of SiC doped with boron [54]. The tiles were coated with graphite to retain a weak interface after

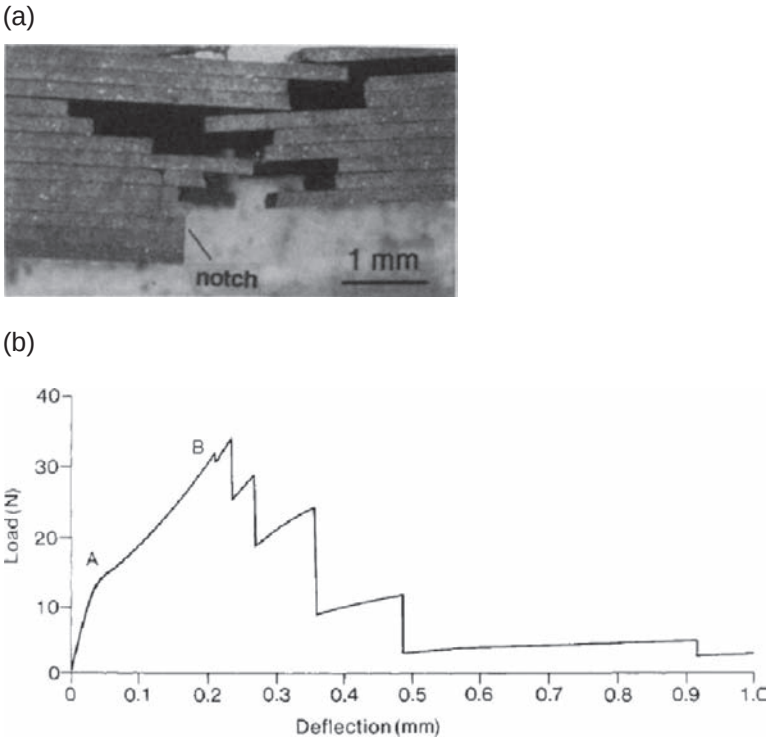

Fig. 19.14. (**a**) The fracture surface of a laminate composite specimen under three-point bending. The role of the interface in deflecting cracks can be clearly seen. (**b**) The load-deflection curve of the specimen. Crack growth begins at *A*, and is followed by a rising load for further deflection till *B* when crack growth becomes more rapid. Reproduced with permission from [54]

sintering. Under a three-point bending test, the crack is deflected along the weak interfaces, preventing catastrophic failure [Fig. 19.14(a)]. The load-deflection curve in Fig. 19.14(b) shows the load continuing to rise after crack growth starts. The laminated composite exhibited a toughness and work of fracture increase by factors of 5 and 100 over monolithic SiC, respectively.

Another larger-scale composite system used alumina tablets of about 50–76 mm long and 1 mm in thickness for the ceramic phase [55]. The plates were bonded with thin adhesive transfer tapes at the interfaces so that the composites achieved 70–90% volume fraction of the ceramic phase. The adhesive exhibited good resilience and extensive ligament formation [Fig. 19.15(a)], contributing to the toughness of the composite. Figure 19.15(b) shows the load-deflection curves of three sets of composite beams from four-point bending tests. The composites with continuous layers and segmented layers with 82 vol.% ceramic showed limited deflections before failure. However, the composite beam with 89 vol.% ceramic exhibited an extensive

(a)

(b)

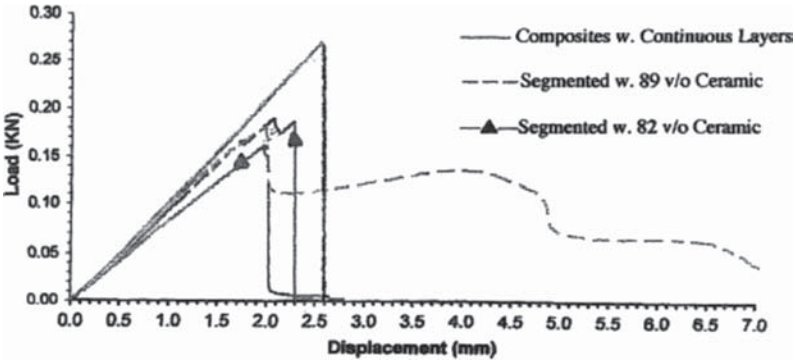

Fig. 19.15. (**a**) A beam being deflected in bending, showing tenacious ligament formation in the adhesive between the platelets. (**b**) Load-displacement curve from four-point bending tests of laminated composites. Reproduced with permission from [55]

deflection with a toughness six-times that of a monolithic alumina beam. The study indicates that a resilient, highly extensible interphase together with a segmented layered microstructure with an optimal ceramic volume fraction is required to achieve maximal toughening.

19.4.2 Ice Templation

Deville et al. utilized the physics of ice formation to develop layered-hybrid materials [56]. By freezing concentrated suspensions containing ceramic particles using precisely controlled freezing kinetics, a homogenous, layered, porous scaffold could

be built. The porous scaffolds were then filled with a second phase, either organic or inorganic, to fabricate dense layered composites.

The freeze-casting process involves the controlled unidirectional freezing of ceramic suspensions. While the ceramic slurry is freezing, the growing ice crystals expel the ceramic particles, causing them to concentrate in the space between the ice crystals (Fig. 19.16). The ice is then sublimated by freeze drying, leaving a ceramic scaffold. The layers of the ice-templated (IT) scaffold are parallel to each other and very homogeneous throughout the entire sample [Fig. 19.17(a)]. A finer microstructure can be obtained by increasing the freezing rate, and a layer thickness of $1\,\mu\mathrm{m}$ could be achieved. Particles trapped in between the ice dendrites lead to a surface roughness of the layers as seen in nacre, while some of the rough asperities span the channels between the lamellae, mimicking the mineral bridges of nacre.

These porous scaffolds are filled with a selected second phase, either organic (epoxy) or inorganic (metal), to fabricate dense composites. The layered composite structure exhibited extensive crack deflection at the interface between layers, leading to increased toughness. The reported toughness of Alumina/Al-Si composite is about $5.5\,\mathrm{MPa\ m^{1/2}}$. Compared with the fracture toughness of aluminum oxide usually in

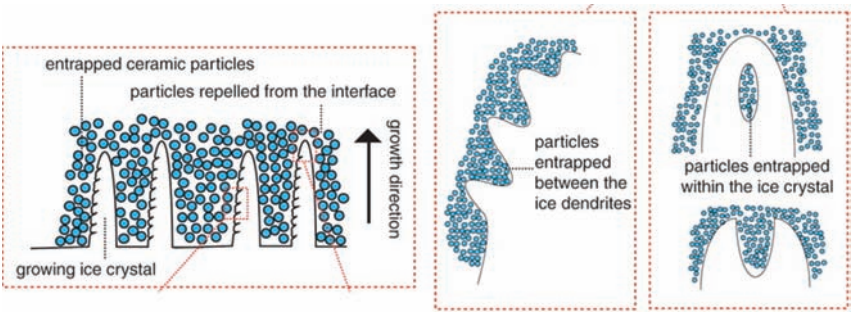

Fig. 19.16. Processing principles for ice templation. While the ceramic slurry is freezing, the growing ice crystals expel the ceramic particles, creating a lamellar microstructure oriented parallel to the direction of the freezing front. A small fraction of particles are entrapped within the ice crystals by tip splitting, leading to the formation of inorganic bridges and roughness on the walls. Reproduced with permission from [56]

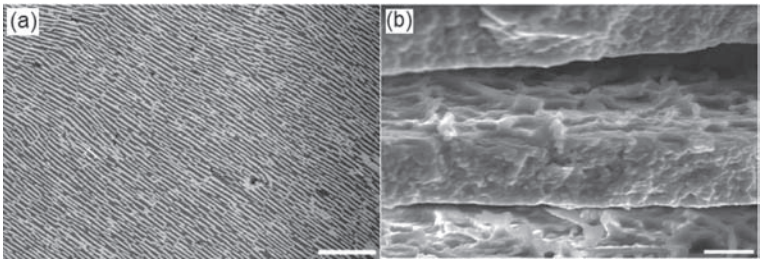

Fig. 19.17. (**a**) The layered microstructure of the IT dense composite (alumina-Al-Si composite). (**b**) The particles entrapped between the ice dendrites generate a characteristic roughness on the lamellar surface that mimics that of nacre. Reproduced with permission from [56]

the range of 3–5 MPa $m^{1/2}$, the increase in toughness is quite modest. The interface chemistry could be modified by adding 0.5 wt.% Ti to the aluminum alloy, which increased the fracture toughness further to 10 MPa $m^{1/2}$. Therefore, the IT process allows a measure of control over the morphology of the inorganic layers and the chemistry of the interface, as well as the ability to build mesostructural features and gradients into the structure, but the improvement of the fracture toughness seems to be limited.

19.4.3 Layer-by-Layer Deposition

A more conventional approach to making artificial nacre is by sequential deposition of organic and inorganic layers. Tang and coworkers used montmorillonite clay tablets (C) and PDDA polyelectrolytes (P), layering them by sequential adsorption of organic and inorganic dispersions in a method called layer-by-layer assembly [57]. The process consists of P-adsorption, rinsing, C-adsorption, and rinsing; repeating this process n times results in the $(P/C)_n$ multilayers. The thickness of each clay platelet is 0.9 nm, and a multilayer with $n = 100$ has a thickness of $2.4\,\mu m$, three orders of magnitude smaller than the characteristic dimensions of nacre.

Strong attractive electrostatic and van der Waals interactions exist between the negatively charged clay tablets and positive polyelectrolytes. During the adsorption step, the clay platelets tend to orient parallel to the surface in order to maximize the attractive energy. Irregular weakly adsorbed platelets are removed during the rinsing step. This results in a high degree of ordering of the microstructure, with the clay sheets strongly overlapping each other, as seen in Fig. 19.18.

The deformation of the multilayers under tension was homogenous, with no dilation bands between the tablets as observed in nacre. This difference was attributed to the extensive overlap of the clay sheets as well as the nanoscale nature of the $(P/C)_n$. The layered composite displayed an abrupt hardening after an initial plastic deformation as shown in Fig. 19.19(a). This was attributed to the stretching of the PDDA molecules from their initial tightly coiled configuration [Fig. 19.19(b)], and the subsequent breaking of P–C ionic bonds as the clay platelets slide over each other.

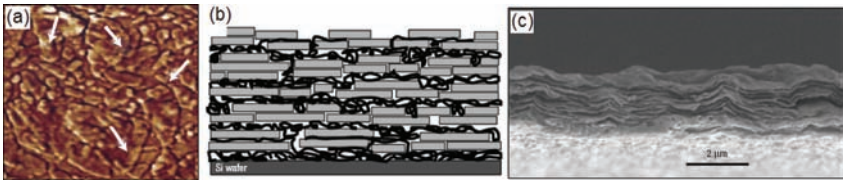

Fig. 19.18. The microscopic structure of the $(P/C)_n$ multilayers. (**a**) Phase-contrast AFM image of a $(P/C)_1$ film. The *arrows* mark the overlap of clay platelets. (**b**) A schematic of the $(P/C)_n$ structure. Note that n describes the number of deposition cycles rather than the number of layers, since several C–P layers may be deposited in each cycle. The thickness of each clay platelet is 0.9 nm. (**c**) SEM image of an edge of a $(P/C)_{100}$ film. Reproduced with permission from [57]

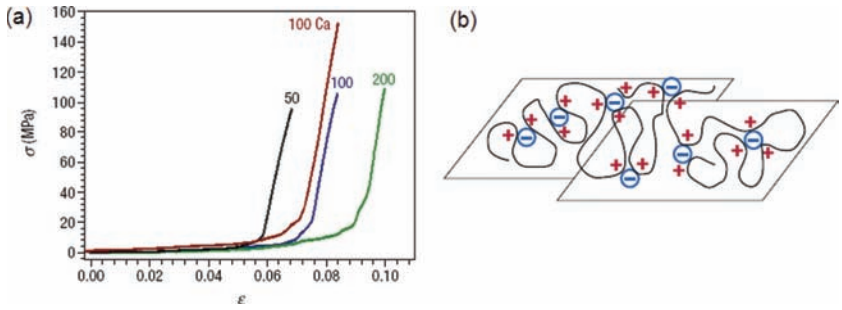

Fig. 19.19. (**a**) Stress-strain curves of free standing films $(P/C)_{50}$, $(P/C)_{100}$, $(P/C)_{200}$, and $(P/C)_{100}$ ion exchanged with Ca^{2+} ions. (**b**) Polyelectrolyte folding and P–C ion pair formation. Reproduced with permission from [57]

Although $(P/C)_n$ the multilayers system exhibited high ultimate tensile properties of $\sigma_u = 100\,\mathrm{MPa}$ and $\varepsilon_u = 0.08$, and the segmented layered composite structure is characteristic of that in nacre, the deformation behavior is quite different from that observed in nacre as inferred from the stress-strain behavior shown in Fig. 19.19(a). In addition, the reliance on the strong attraction between the constituents limits the application of the method to a narrow range of materials.

19.4.4 Thin Film Deposition: MEMS-Based Structure

While a lot of effort has been put into reproducing the layered structure of nacre, an attempt was made recently for the first time to mimic the crossed-lamellar microstructure of the Queen conch (*Strombus gigas*), using MEMS (microelectromechanical systems) technology [11]. Polysilicon and photoresist were chosen as substitutes for aragonite and the organic matrix, and the microstructure was fabricated as a stack of three consecutively deposited films, the designs of which are shown in Fig. 19.20.

Each film is an approximation of the inner (or outer) and middle layers of the *Strombus gigas* shell, covering two length scales. The bottom half represents the inner layer with vertical interfaces, while the top half represents the middle layer with the interfaces oriented at $\pm 45°$ to the horizontal. The films are deposited so that the angled interfaces are oriented in alternating directions designed to make the middle layer tougher than the inner layer.

The fabrication makes use of standard MEMS technology, repeating the deposition of a thin silicon film ($\sim 2\,\mu\mathrm{m}$) on which trenches for the interfaces are etched out with RIE (reactive ion etching) which are in turn filled with photoresist. Mechanical tests were performed as shown in Fig. 19.21. The results revealed that the micro-composite displayed significant ductility and toughness compared to monolithic silicon, with an estimated increase in energy dissipation of 36-times that for silicon. However, the energy-dissipation mechanisms were slightly different from those of the mollusk shell. Rather than the multiple tunnel cracking seen in the *Strombus gigas* shells, the micro-composite showed extensive delamination between the three

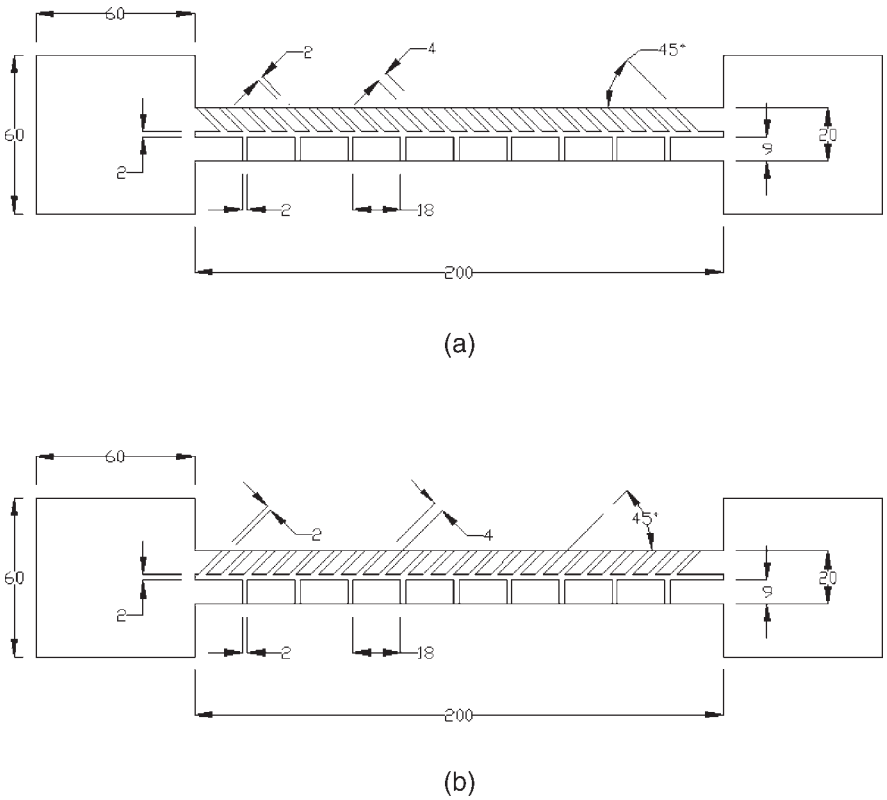

Fig. 19.20. Top view of designed structural geometry: (**a**) first and third film and (**b**) second film in the three-film stack. Dimensions are in μm. Reproduced with permission from [11]

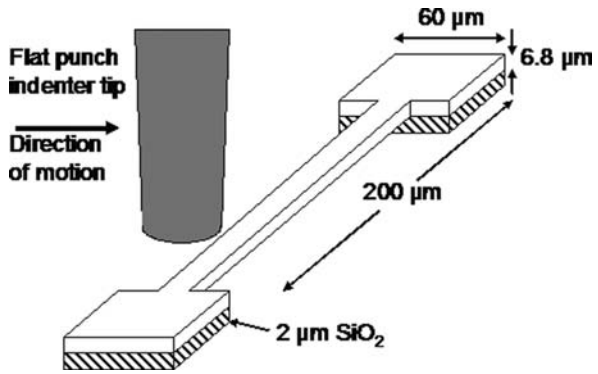

Fig. 19.21. Schematic illustration of a mechanical test. The load was applied in the lateral direction with a punch with a flat tip equipped with a lateral displacement transducer. Reproduced with permission from [11]

stacks. This could be due to the fact that the ratio of thickness of the interface ($2\,\mu m$) to thickness of the lamellae ($4\,\mu m$) is much larger than what is found in the structure of the conch shell. However, the bridged cracks along the $\pm 45°$ interfaces in the middle layer were similar to those seen in the Queen conch shells, and the microcomposite demonstrated a significant increase in strength and work of fracture.

19.5 Conclusions

Much progress has been made in characterizing the structure and mechanical properties of mollusk shells. However, a number of issues remain unresolved. In particular, the specific roles of nanograins, mineral bridges, and nanoasperities in nacre need further investigation. Likewise, general constitutive laws for these materials along various loading paths are currently unavailable.

Advances in in-situ microscopy experiments along with detailed multiscale modeling will facilitate and enhance our understanding of the relationship between material microstructure and mechanical properties.

In the manufacturing of artificial shell materials, creative and innovative methods are emerging. However, much work remains in order to obtain the morphological and chemical control of the interface needed to achieve the performance exhibited by mollusk shells. One lesson from studying these materials is that the desirable inelastic deformation mechanisms are the result of complex synergies between the constituents and the hierarchical structural features. Therefore, biomimicking of mollusk shells requires the optimum selection of constituent materials and manufacturing approaches to materialize the mechanistic synergies. It is anticipated that experiments and modeling will continue to be vital in addressing this challenge.

References

1. Sarikaya M, Aksay IA, (eds) (1995) Biomimetics, Design and Processing of Materials. Woodbury, NY.
2. Mayer G (2005) Rigid biological systems as models for synthetic composites. Science, 310(5751):1144–1147.
3. Wegst UGK, Ashby MF (2004) The mechanical efficiency of natural materials. Philos Mag 84(21):2167–2181.
4. Currey JD (1999) The design of mineralised hard tissues for their mechanical functions. J Exp Biol 202(23):3285–3294.
5. Gao HJ, Ji BH, Jager IL, Arzt E, Fratzl P (2003) Materials become insensitive to flaws at nanoscale: lessons from nature. Proc Natl Acad Sci USA 100(10):5597–5600.
6. Ballarini R, Kayacan R, Ulm FJ, Belytschko T, Heuer AH (2005) Biological structures mitigate catastrophic fracture through various strategies. Int J Fract 135(1–4):187–197.
7. Kohn AJ (2002) Encyclopedia of evolution: Mollusks. Oxford Unversity Press.
8. Currey JD, Taylor JD (1974) The mechanical behavior of some Molluskan hard tissues. J Zool (London), 173(3):395–406.
9. Kamat S, Su X, Ballarini, R, Heuer AH (2000) Structural basis for the fracture toughness of the shell of the conch *Strombus gigas*. Nature 405(6790):1036–1040.

10. Su XW, Zhang DM, Heuer AH (2004) Tissue regeneration in the shell of the giant queen conch, *Strombus gigas*. Chem Mater 16(4):581–593.
11. Chen L, Ballarini R, Kahn H, Heuer AH (2007) Bioinspired micro-composite structure. J Mater Res 22(1):124–131.
12. Currey JD, Kohn AJ (1976) Fracture in crossed-lamellar structure of Conus Shells. J Mater Sci 11(9):1615–1623.
13. KuhnSpearing LT, Kessler H, Chateau E, Ballarini R, Heuer AH, Spearing SM (1996) Fracture mechanisms of the *Strombus gigas* conch shell: implications for the design of brittle laminates. J Mater Sci 31(24):6583–6594.
14. Kessler H, Ballarini R, Mullen RL, Kuhn LT, Heuer AH (1996) A biomimetic example of brittle toughening .1. Steady state multiple cracking. Comput Mater Sci 5(1–3):157–166.
15. Cox BN, Marshall DB (1994) Overview no 111 – concepts for bridged cracks in fracture and fatigue. Acta Metall Mater 42(2):341–363.
16. Kamat S, Kessler H, Ballarini R, Nassirou M, Heuer AH (2004) Fracture mechanisms of the *Strombus gigas* conch shell: II – Micromechanics analyses of multiple cracking and large-scale crack bridging. Acta Mater 52(8):2395–2406.
17. Aveston J, Cooper GA, Kell A (1971) Properties of fiber composites. Conference Proceedings 15, National Physical Laboratory, IPC Science and Technology Press.
18. Jackson AP, Vincent JFV, Turner RM (1988) The mechanical design of nacre. Proc R Soc London 234(1277):415–440.
19. Wang RZ, Suo Z, Evans AG, Yao N, Aksay IA (2001) Deformation mechanisms in nacre. J Mater Res 16:2485–2493.
20. Kotha SP, Li Y, Guzelsu N (2001) Micromechanical model of nacre tested in tension. J Mater Sci 36(8):2001–2007.
21. Barthelat F, Tang H, Zavattieri PD, Li CM, Espinosa HD (2007) On the mechanics of mother-of-pearl: a key feature in the material hierarchical structure. J Mech Phys Solids 55(2):225–444.
22. Evans AG, Suo Z, Wang RZ, Aksay IA, He MY, Hutchinson JW (2001) Model for the robust mechanical behavior of nacre. J Mater Res 16(9):2475–2484.
23. Smith BL, Schaeffer TE, Viani M, Thompson JB, Frederick NA, Kindt J, Belcher A, Stucky GD, Morse DE, Hansma PK (1999) Molecular mechanistic origin of the toughness of natural adhesives, fibres and composites. Nature (London), 399(6738):761–763.
24. Song F, Bai YL (2003) Effects of nanostructures on the fracture strength of the interfaces in nacre. J Mater Res 18:1741–1744.
25. Meyers MA, Lin AYM, Chen PY, Muyco J (2008) Mechanical strength of abalone nacre: role of the soft organic layer. J Mech Behaiv Biomed Mater 1(1):76–85.
26. Su XW, Belcher AM, Zaremba CM, Morse DE, Stucky GD, Heuer AH (2002) Structural and microstructural characterization of the growth lines and prismatic microarchitecture in red abalone shell and the microstructures of abalone “flat pearls”. Chem Mater 14(7):3106–3117.
27. Lin A, Meyers MA (2005) Growth and structure in abalone shell. Mater Sci Eng A Struct Mater 390(1–2):27–41.
28. Barthelat F, Tang H, Zavattieri PD, Li, CM, Espinosa HD (2007) On the mechanics of mother-of-pearl: a key feature in the material hierarchical structure. J Mech Phys of Solids 55(2):306–337.
29. Blank S, Arnoldi M, Khoshnavaz S, Treccani L, Kuntz M, Mann K, Grathwohl G, Fritz M (2003) The nacre protein perlucin nucleates growth of calcium carbonate crystals. J Microsc Oxford 212:280–291.
30. Feng QL, Cui FZ, Pu G, Wang RZ, Li HD (2000) Crystal orientation, toughening mechanisms and a mimic of nacre. Mater Sci Eng C Biomimetic Supramol Syst 11(1):19–25.

31. Manne S, Zaremba CM, Giles R, Huggins L, Walters DA, Belcher A, Morse DE, Stucky GD, Didymus JM, Mann S, Hansma, PK (1994) Atomic-force microscopy of the nacreous layer in mollusk shells. Proc R Soc London Ser B-Biol Sci 256(1345):17–23.
32. Song F, Zhang XH, Bai YL (2002) Microstructure in a biointerface. J Mater Sci Lett 21:639–641.
33. Bruet BJF, Qi HJ, Boyce MC, Panas R, Tai K, Frick L, Ortiz C (2005) Nanoscale morphology and indentation of individual nacre tablets from the gastropod mollusk *Trochus niloticus*. J Mater Res 20(9):2400–2419.
34. Barthelat F, Li CM, Comi C, Espinosa HD (2006) Mechanical properties of nacre constituents and their impact on mechanical performance. J Mat Res 21(8):1977–1986.
35. Li XD, Chang WC, Chao YJ, Wang RZ, Chang M (2004) Nanoscale structural and mechanical characterization of a natural nanocomposite material: the shell of red abalone. Nano Lett 4(4):613–617.
36. Rousseau M, Lopez E, Stempfle P, Brendle M, Franke L, Guette A, Naslain R, Bourrat X (2005) Multiscale structure of sheet nacre. Biomaterials 26(31):6254–6262.
37. Schaeffer TE, IonescuZanetti C, Proksch R, Fritz M, Walters DA, Almqvist N, Zaremba CM, Belcher AM, Smith BL, Stucky GD, Morse DE, Hansma PK (1997) Does abalone nacre form by heteroepitaxial nucleation or by growth through mineral bridges? Chem Mater 9(8):1731–1740.
38. Lin AYM, Chen PY, Meyers MA (2008) The growth of nacre in the abalone shell. Acta Biomater, 4:131–138.
39. Currey JD (1977) Mechanical properties of mother of pearl in tension. Proc R Soc London 196(1125):443–463.
40. Barthelat F, Espinosa HD (2007) An experimental investigation of deformation and fracture of nacre-mother of pearl. Exp Mech 47(3):311–324.
41. Menig R, Meyers MH, Meyers MA, Vecchio KS (2000) Quasi-static and dynamic mechanical response of *Haliotis rufescens* (abalone) shells. Acta Mater 48.
42. Barthelat F, Espinosa HD (2005) Mechanical Properties of Nacre Constituents: an inverse method approach. MRS 2004 Fall Meeting Boston.
43. Katti DR, Katti KS (2001) Modeling microarchitecture and mechanical behavior of nacre using 3D finite element techniques. Part 1. Elastic properties. J Mater Sci 36:1411–1417.
44. Li XD, Xu ZH, Wang RZ (2006) In situ observation of nanograin rotation and deformation in nacre. Nano Lett 6(10):2301–2304.
45. Ji BH, Gao HJ (2004) Mechanical properties of nanostructure of biological materials. J Mech Phys Solids 52(9):1963–1990.
46. Lawn BR (1993) Fracture of Brittle Solids. Cambridge University Press, New York.
47. Kruzic J, Nalla RK, Kinney JH, Ritchie RO (2003) Crack blunting, crack bridging and resistance-curve fracture mechanics in dentin: effect of hydration. Biomaterials 24(28):5209–5221.
48. Nalla RK, Kruzic JJ, Kinney JH, Ritchie RO (2005) Mechanistic aspects of fracture and R-curve behavior in human cortical bone. Biomaterials 26(2):217–231.
49. Budiansky B, Hutchinson JW, Lambropoulos JC (1983) Continuum theory of dilatant transformation toughening in ceramics. Int J Solids Struct 19(4):337–355.
50. Evans AG, Ahmad ZB, Gilbert DG, Beaumont PWR (1986) Mechanisms of toughening in rubber toughened polymers. Acta Metall 34(1):79–87.
51. Du J, Thouless MD, Yee AF (1998) Development of a process zone in rubber-modified epoxy polymers. International J Fract 92(3):271–285.
52. Evans AG, Hutchinson JW (1989) Effects of non-planarity on the mixed-mode fracture-resistance of bimaterial interfaces. Acta Metall 37(3):909–916.
53. Evans AG (1990) Perspective on the development of high-toughness ceramics. J Am Ceram Soc 73(2):187–206.

54. Clegg WJ, Kendall K, Alford NM, Button TW, Birchall JD (1990) A simple way to make tough ceramics. Nature 347(6292):455–457.
55. Mayer G (2006) New classes of tough composite materials – lessons from natural rigid biological systems. Mater Sci Eng C Biomimetic Supramol Syst 26(8):1261–1268.
56. Deville S, Saiz E, Nalla RK, Tomsia AP (2006) Freezing as a path to build complex composites. Science 311(5760):515–518.
57. Tang ZY, Kotov NA, Magonov S, Ozturk B (2003) Nanostructured artificial nacre. Nat Mater 2(6):413–U418.